

## Article

# A Quantum-Mechanical Study of Antiphase Boundaries in Ferromagnetic B2-Phase Fe<sub>2</sub>CoAl Alloy

Martin Friák <sup>1,\*</sup> , Josef Gracias <sup>2</sup>, Jana Pavlů <sup>2</sup>  and Mojmír Šob <sup>2,1</sup> 

<sup>1</sup> Institute of Physics of Materials, v.v.i., Czech Academy of Sciences, Žitkova 22, CZ-616 00 Brno, Czech Republic

<sup>2</sup> Department of Chemistry, Faculty of Science, Masaryk University, Kotlářská 2, CZ-611 37 Brno, Czech Republic; 461108@mail.muni.cz (J.G.); houserova@chemi.muni.cz (J.P.); sob@chemi.muni.cz (M.Š.)

\* Correspondence: friak@ipm.cz

**Abstract:** In this study, we performed a quantum mechanical examination of thermodynamic, structural, elastic, and magnetic properties of single-phase ferromagnetic Fe<sub>2</sub>CoAl with a chemically disordered B2-type lattice with and without antiphase boundaries (APBs) with (001) crystallographic orientation. Fe<sub>2</sub>CoAl was modeled using two different 54-atom supercells with atoms on the two B2 sublattices distributed according to the special quasi-random structure (SQS) concept. Both computational models exhibited very similar formation energies (−0.243 and −0.244 eV/atom), B2 structure lattice parameters (2.849 and 2.850 Å), magnetic moments (1.266 and 1.274 μ<sub>B</sub>/atom), practically identical single-crystal elastic constants (C<sub>11</sub> = 245 GPa, C<sub>12</sub> = 141 GPa, and similar C<sub>44</sub> = 132 GPa) and auxetic properties (the lowest Poisson ratio close to −0.1). The averaged APB interface energies were observed to be 199 and 310 mJ/m<sup>2</sup> for the two models. The studied APBs increased the total magnetic moment by 6 and 8% due to a volumetric increase as well as local changes in the coordination of Fe atoms (their magnetic moments are reduced for increasing number of Al neighbors but increased by the presence of Co). The APBs also enhanced the auxetic properties.

**Keywords:** Fe<sub>2</sub>CoAl; disorder; antiphase boundaries; elasticity; magnetism; ab initio; auxetic



**Citation:** Friák, M.; Gracias, J.; Pavlů, J.; Šob, M. A Quantum Mechanical Study of Antiphase Boundaries in Ferromagnetic B2-Phase Fe<sub>2</sub>CoAl Alloy. *Magnetochemistry* **2021**, *7*, 137. <https://doi.org/10.3390/magnetochemistry7100137>

Academic Editors: Masami Tsubota and Jiro Kitagawa

Received: 28 August 2021

Accepted: 30 September 2021

Published: 9 October 2021

**Publisher's Note:** MDPI stays neutral with regard to jurisdictional claims in published maps and institutional affiliations.



**Copyright:** © 2021 by the authors. Licensee MDPI, Basel, Switzerland. This article is an open access article distributed under the terms and conditions of the Creative Commons Attribution (CC BY) license (<https://creativecommons.org/licenses/by/4.0/>).

## 1. Introduction

Ternary X<sub>2</sub>YZ materials with Heusler-type crystal lattice [1] include numerous combinations of different chemical elements. Their properties have been very intensively studied [2,3], including their magnetic properties [4–6], half-metallic features [7–11], magneto-optical properties [12], topological quantum properties [13,14], and shape memory features [15,16]. Regarding theoretical studies, there are two high-throughput studies conducted by Gilleßen and Dronskowski of 810 different ternary compounds with either the full [17] or inverse [18] Heusler structure.

Our study is focused on Fe<sub>2</sub>CoAl belonging to a very promising class of materials based on Fe and Al [19–26]. Earlier experimental studies [27–37] are currently complemented by research efforts related to applications in high-temperature coatings [38–44] and composites [45–49], new preparation techniques [50–53] and their material properties [54,55]. Theoretical studies of iron aluminides include ab initio calculations of single-phase materials [56–65] and nanocomposites [66,67], analyses of their magnetic characteristics [68,69], combined methodological approaches [70–73], and calculations of properties of defects [74–79]. We used a structural model based on the experimental work of Grover et al. [80], where a single-phase Fe<sub>2</sub>CoAl has a chemically disordered B2 lattice with one sublattice containing equal amounts of Fe and Co and the second sublattice equal amounts of Fe and Al. We employed ab initio calculations to study properties of both defect-free states and those containing antiphase boundaries (APBs) with (001)

crystallographic orientation. APBs are extended defects commonly found in Fe-Al-based compounds [81–86] and have also been theoretically studied [87–95].

## 2. Methods

When modeling a partially disordered B2-phase of Fe<sub>2</sub>CoAl, we utilized two different 54-atom supercells (see Figure 1a,b) with the atoms on the two sublattices distributed according to the special quasi-random structure (SQS) concept [96] and generated using USPEX software [97–99]. The actual stoichiometry of our supercells Fe<sub>27</sub>Co<sub>14</sub>Al<sub>13</sub> and Fe<sub>2</sub>Co<sub>1.037</sub>Al<sub>0.963</sub> slightly deviates from the exact Fe<sub>2</sub>CoAl stoichiometry in favor of Co and at the expense of Al, because 54 is not divisible by 4. Cube-shaped 54-atom supercells were chosen as  $3 \times 3 \times 3$  multiples of a 2-atom B2 cell. The two models were then doubled along the [001] direction to obtain 108-atom supercells that we refer to as variant 1 and variant 2; see Figure 1c,d. In order to obtain supercells containing APBs, the atoms in the upper parts of these 108-atom supercells were shifted according to the APB-related  $\langle 111 \rangle$  shift; see red arrows in Figure 1c,d. One atomic plane was cyclically relocated within the shifted parts of the supercells in order to preserve the stoichiometry; see Figure 1e,f. This construction leads to two different APBs per supercell, and, therefore, averaged APB-related characteristics, such as APB interface energy, are computed. One APB is located in the middle of the supercells shown in Figure 1e,f and the other at the top (its image also appears at the bottom due to the periodic boundary conditions). Both APBs differently change the local coordination of atoms (see below).

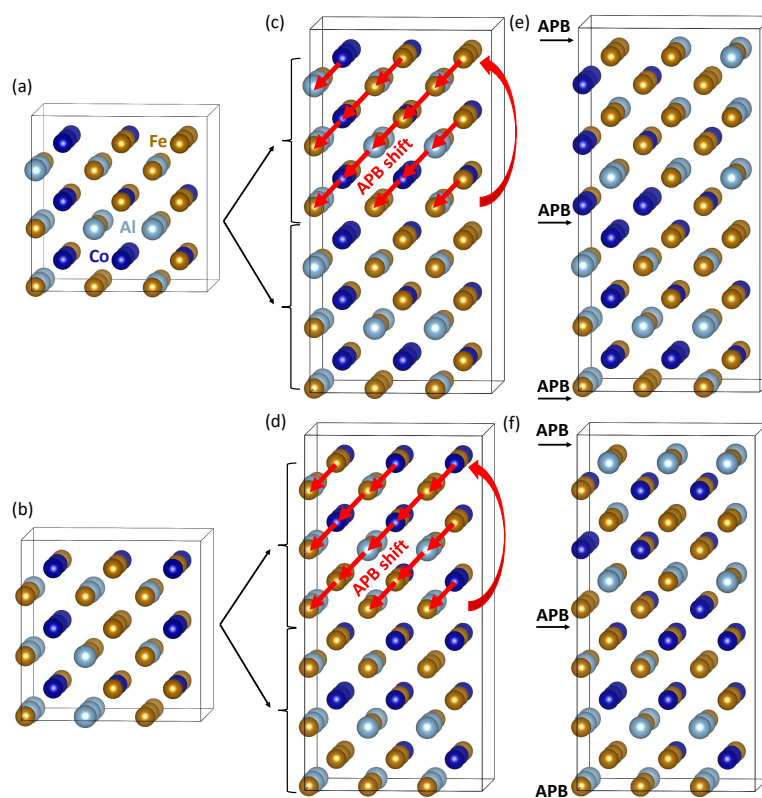


**Figure 1.** A schematic visualization of the computational supercells employed to model Fe<sub>2</sub>CoAl (a small deviation from the exact stoichiometry is discussed in the text). (a,b) show 54-atom supercells, which we refer to as variants 1 and 2, respectively, as special quasi-random models of B2-phase Fe<sub>2</sub>CoAl. (c,d) are doubles of these 54-atom supercells along the [001] direction, respectively. In order to model antiphase boundaries (APBs), we applied APB-related  $\langle 111 \rangle$  shift marked by red arrows in (c,d) and obtained supercells shown in (e,f). To preserve the stoichiometry of the supercells when applying the APB shift to the upper half of 108-atom supercells in (c,d), one atomic plane was cyclically relocated to the top of each supercell; see red curved arrow in (c,d).

Our ab initio calculations were performed employing the Vienna Ab initio Simulation Package (VASP) [100,101] that implements density functional theory [102,103]. For parametrization, we used projector-augmented wave (PAW) pseudopotentials [104,105] and generalized gradient approximation (GGA) developed by Perdew and Wang [106] (PW91) with Vosko–Wilk–Nusair correction [107]. Our setup was chosen as it correctly predicts the ground state of Fe<sub>3</sub>Al (a binary variant of Fe<sub>2</sub>CoAl) to be the D0<sub>3</sub> structure (its energy is lower than that of Fe<sub>3</sub>Al with the L1<sub>2</sub> structure by about 5.5 meV/atom [108]). Our calculations were performed with a plane wave energy cut-off of 400 eV. The product of (i) the number of Monkhorst–Pack k-points and (ii) the number of atoms was equal to 27,648 (e.g., 8 × 8 × 4 k-point mesh in the case of 108-atom supercells in Figure 1c–f). We fully relaxed all studied supercells; i.e., the energy and forces were minimized with respect to atomic positions, cell shape, and volume (forces acting upon atoms were reduced under 0.01 eV/Å). All local magnetic moments of Fe and Co atoms were ferromagnetic. The formation energies discussed below were evaluated with respect to ferromagnetic bcc Fe, ferromagnetic hcp Co, and non-magnetic fcc Al, which were computed with the same cut-off energy and similar k-point densities.

### 3. Results

Regarding our two 54-atom computational models of B2-phase Fe<sub>2</sub>CoAl, their computed thermodynamic, structural, and magnetic properties are listed in Table 1. The formation energies of both variants are very similar, −0.243 and −0.244 eV/atom, despite the apparently very different distribution of atoms (see Figure 1a,b), and we interpreted our findings as a proof of the quality of the used computational models. The above discussed formation energy is very close to that obtained in our previous study [109] (−0.269 eV/atom) for a smaller 16-atom supercell with partly disordered B2-phase sublattices. A small difference between the values is likely due to the fact that the 16-atom supercells used in our previous studies [109,110] allowed us to capture the exact Fe<sub>2</sub>CoAl stoichiometry, while the 54-atom supercells used in the current study are slightly off-stoichiometric Co-rich Fe<sub>2</sub>Co<sub>1.037</sub>Al<sub>0.963</sub> materials as mentioned above. The 16-atom supercells are, on the other hand, quite small for proper modeling of disordered systems, their tensorial elastic properties in particular [111], and this is why we used larger supercells in our current study. B2 structure lattice parameters (2.849 and 2.850 Å), and magnetic moments (1.266 and 1.274 μ<sub>B</sub> per atom) of these two models are very similar and in agreement with experimental values (that are unfortunately available only for a completely disordered A2 phase). Table 1 also contains computed properties of systems with APBs. The APB interface energies (averaged over two different APB interfaces) for the two supercells, variants 1 and 2, are equal to 199 and 310 mJ/m<sup>2</sup>, respectively.

**Table 1.** Calculated formation energy  $E_f$ , volume per atom  $V$ , a two-atom B2 lattice parameter  $a^{B2}$ , tetragonality ratio  $c/a$  (the lattice parameter  $c$  is perpendicular to the APB interfaces), magnetic moment  $\mu$  per atom, and the averaged APB interface energy  $\langle\gamma^{APB}\rangle$  for supercells with APBs.

Structure	$E_f$	$V$	$a^{B2}$	$c/a$	$\mu$	$\langle\gamma^{APB}\rangle$
	eV/atom	Å <sup>3</sup> /atom	Å		μ <sub>B</sub> /atom	mJ/m <sup>2</sup>
var. 1 no APBs	−0.243	11.56	2.849	1.000	1.266	—
var. 1 with APBs	−0.226	11.65	—	1.011	1.344	199
exp. A2-phase [112]	—	11.77	2.866	1.000	1.18–1.23	—
var. 2 no APBs	−0.244	11.58	2.850	1.000	1.274	—
var. 2 with APBs	−0.218	11.72	—	1.006	1.380	310

As far as the structure is concerned, the studied APBs have a multiple effect. First, the volume per atom is increased from 11.56 to 11.65 Å<sup>3</sup> and from 11.58 to 11.72 Å<sup>3</sup> for supercell variants 1 and 2, respectively. Second, the  $c/a$  ratio of lattice parameters perpendicular and

parallel to the APB interfaces slightly deviates from 1.000 (for a cubic-symmetry system) by 1.1% and 0.6% for variants 1 and 2, respectively.

As far as single-crystal elastic properties are concerned, the calculated values are summarized in Table 2. It is worth mentioning that the anisotropic elastic properties of our computational supercells as models for a disordered state of Fe<sub>2</sub>CoAl are not exactly equal along certain directions, for example, [100], [010] and [001] crystallographic directions. The differences are small, about 1–2 GPa with respect to the values of about 150 GPa. Nevertheless, we used the rigorous mathematical treatment developed by Moakher and Norris [113] to determine the closest cubic-symmetry elastic tensor, and its components are listed in Table 2. As far as our two models for the B2-phase Fe<sub>2</sub>CoAl are concerned, the elastic constants  $C_{11}$ ,  $C_{12}$ , and  $C_{44}$  for the two supercells, variant 1 and variant 2, are practically identical (with differences within an expected error bar of our calculations, that is, about 1–2 GPa). The anisotropy of the elastic response is visualized in the form of directional dependencies of the single-crystal Young's modulus in Figure 2a. Using ELATE software [114] to produce these figures, we also determined the minimum and maximum values of single-crystal Young's modulus  $Y$ , shear modulus  $G$ , and Poisson's ratio  $\nu$ . Interestingly, our analysis predicts that Fe<sub>2</sub>CoAl is an auxetic material; i.e., the Poisson ratio is negative for certain directions of loading—see the negative values of  $\nu_{\min}$  in Table 2. Figure 2c shows directional dependences of the both maximum and minimum value of Poisson ratio (for details, see Ref. [114]), and Figure 2d visualizes these trends within the (x,z) plane with negative values marked by red colors (selected examples are highlighted by red arrows).

The impact of APBs on elastic properties is minimal. The elastic constant  $C_{11}$ , as well as  $C_{33}$  due to the tetragonal symmetry of the APB-containing systems, is slightly lower (by a few percent), but other elastic constants are nearly unaffected. The impact of APBs on elastic properties is well demonstrated in the case of elastic characteristics of polycrystals. We evaluated them from the single-crystal elastic constants listed in Table 2, employing ELATE software [114] (open-access at <http://progs.coudert.name/elate>, accessed date 29 September 2021). The values obtained when using Voigt [115], Reuss [116] and Hill [117] homogenization methods are summarized in Table 3, and the APB-related changes are lower than 10%.

**Table 2.** Calculated single-crystal elastic constants of variants 1 and 2 as models of Fe<sub>2</sub>CoAl with and without APBs. The values of  $C_{11}$ ,  $C_{33}$ ,  $C_{12}$ ,  $C_{13}$ ,  $C_{44}$ ,  $C_{66}$ , Young's moduli  $Y_{\min}$ ,  $Y_{\max}$ , and shear moduli  $G_{\min}$  and  $G_{\max}$  are given in GPa, and we expect their error bar to be 1–2 GPa. The minimum and maximum values of  $Y$ ,  $G$ , and  $\nu$  were obtained using ELATE software [114].

Single-Crystal Elastic Constants	$C_{11}$ (GPa)	$C_{33}$ (GPa)	$C_{12}$ (GPa)	$C_{13}$ (GPa)	$C_{44}$ (GPa)	$C_{66}$ (GPa)
var. 1 without APBs	244	244	141	141	131	131
var. 1 with APBs	232	228	138	143	134	132
var. 2 without APBs	247	247	141	141	132	132
var. 2 with APBs	234	227	136	141	133	132
	$Y_{\min}$ (GPa)	$Y_{\max}$ (GPa)	$G_{\min}$ (GPa)	$G_{\max}$ (GPa)	$\nu_{\min}$	$\nu_{\max}$
var. 1 without APBs	141	315	52	131	−0.083	0.626
var. 1 with APBs	117	318	43	134	−0.139	0.728
var. 2 without APBs	145	317	53	132	−0.075	0.614
var. 2 with APBs	120	316	45	133	−0.125	0.715

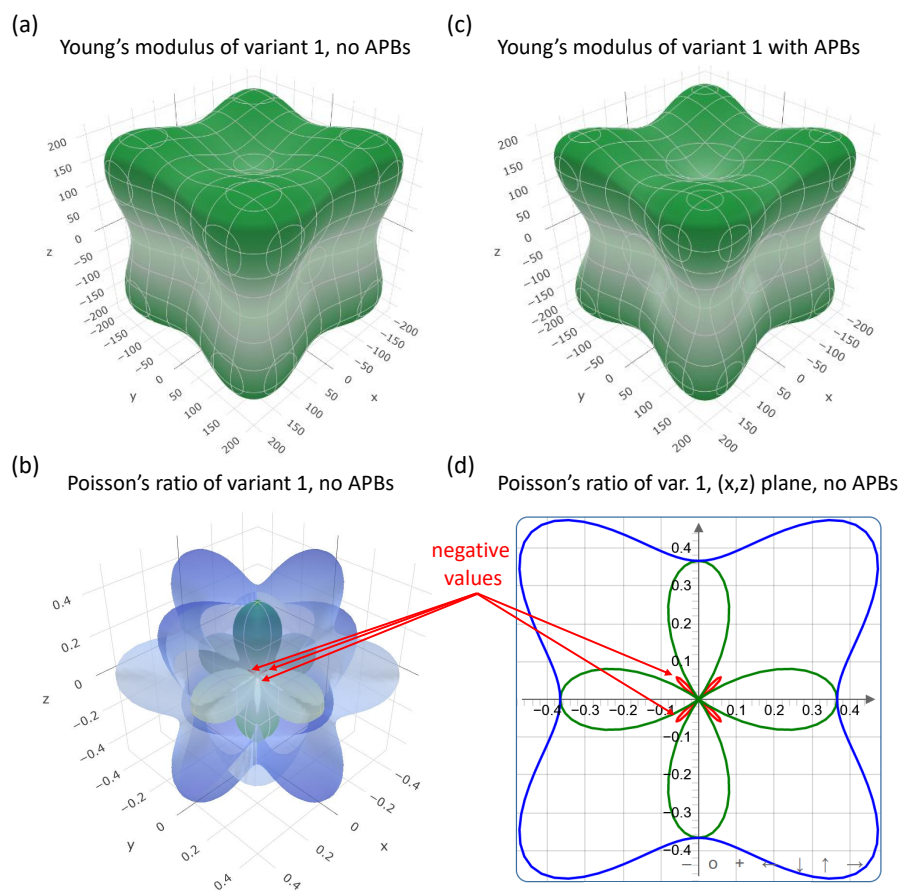


**Figure 2.** Calculated directional dependencies of Young's modulus of supercells modeling  $\text{Fe}_2\text{CoAl}$ , in particular variant 1 (a) without APBs (b) and with APBs. For variant 1 without APBs, we also show a directional dependence of the minimum and maximum value of Poisson's ratio (c) and their behavior within the  $(x,z)$  plane (d), see Ref. [114] for details, with examples of negative values indicated by red arrows. The figures were produced using ELATE software [114] (open-access at <http://progs.coudert.name/elate>, accessed date 29 September 2021).

Importantly, the magnetic moments of APB-containing systems are higher by 6 and 8% for variants 1 and 2, respectively, when compared with their corresponding APB-free states; see Table 1. This increase in magnetism can be partly explained by the above-discussed increase in volume (magneto-volumetric effects), but there are other active mechanisms that require attention (see below).

**Table 3.** Polycrystalline bulk modulus  $B$ , Young's modulus  $Y$ , shear modulus  $G$ , and Poisson's ratio  $\nu$  computed according to Voigt, Reuss, and Hill homogenization methods in the of variants 1 and 2 of  $\text{Fe}_2\text{CoAl}$  with and without APBs as obtained using the ELATE software [114] (open-access at <http://progs.coudert.name/elate>, accessed date 29 September 2021). The expected error bar of the values of the three moduli ( $B$ ,  $Y$  and  $G$ ) is 1–2 GPa.

Polycrystal Elasticity	$B$	$Y$	$G$	$\nu$
	Voigt/Reuss/Hill Values in GPa			Voigt/Reuss/Hill
APB-free var. 1	175/175/175	250/211/231	99/81/90	0.262/0.300/0.281
var. 1 with APBs	171/171/171	247/194/221	98/74/86	0.260/0.311/0.285
APB-free var. 2	176/176/176	253/215/234	100/83/92	0.261/0.297/0.279
var. 2 with APBs	170/170/170	247/198/223	98/76/87	0.258/0.306/0.282

#### 4. Discussion

The enhancement of magnetism due to the studied APBs is significantly more complex at the level of individual atoms. It is schematically shown in Figure 3, where the atoms are represented by spheres with diameter scaling the magnitude of the local magnetic moments. In order to understand these complex states, it is worth discussing the impact of APBs on sublattices within the B2 phase of  $\text{Fe}_2\text{CoAl}$ . This phase contains (according to Grover et al. [80]) one disordered sublattice with equal amounts of Fe and Co atoms and another disordered sublattice with equal amounts of Fe and Al atoms. Schematically we can decompose the chemical formula of  $\text{Fe}_2\text{CoAl}$  into another one that reflects these sublattices,  $\text{Fe}_2\text{CoAl} = (\text{Fe},\text{Co})(\text{Fe},\text{Al})$ . In a state without APBs, the atoms at one sublattice represent the first nearest neighbors (1NN) of atoms from the other sublattice, but the studied APBs change it. At the APB interface in the middle of Figure 1e,f, the atoms at the (Fe,Co) sublattice have newly half of their 1NN atoms from the same (Fe,Co) sublattice.

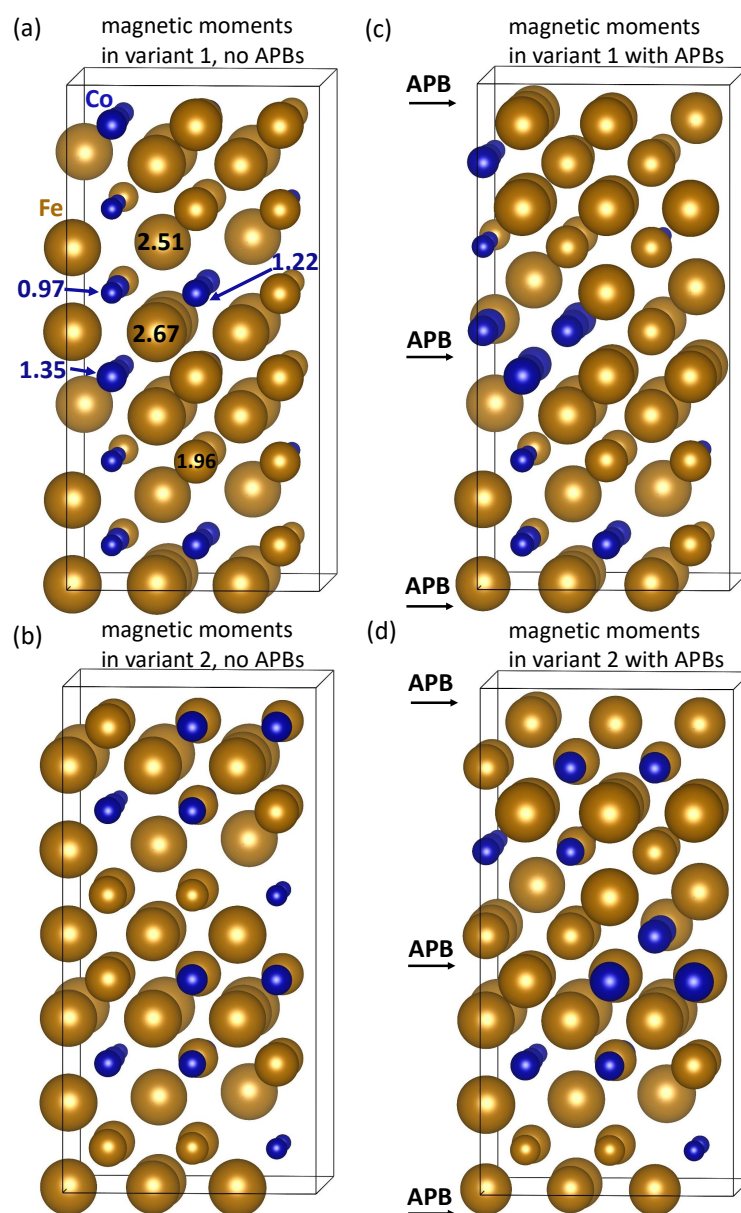


**Figure 3.** Computed local magnetic moments of atoms in supercells modeling  $\text{Fe}_2\text{CoAl}$ , in particular variants 1 and 2 without APBs (a,b), respectively, and variants 1 and 2 with APBs (c,d), respectively. The magnitude of local moments are indicated by the diameter of the spheres representing atoms—examples of the values for a few Fe and Co atoms (in Bohr magnetons) are listed in part (a).

Similarly, at the APB interface at the top/bottom of Figure 1e,f, the atoms at the (Fe,Al) sublattice are coordinated by the atoms from the same sublattice as one half of their 1NN shell. The change in the chemical composition of 1NN shell is essential for the magnetism of atoms. Figure 4 shows the local magnetic moments of either Fe or Co atoms as functions of the number of either Al or Co atoms in the 1NN shell. The local magnetic moments of Fe and Co atoms mostly decrease with an increasing number of Al atoms in their 1NN shell (see Refs. [69,75,94]). On the contrary, the magnetic moments of Fe atoms mostly increase with the increasing number of Co atoms in the 1NN shell of Fe atoms. While it is hard to extract clear trends from Figure 4, the visualized APB-related changes in the coordination of magnetic atoms also contribute into the increase in the total magnetic moment.

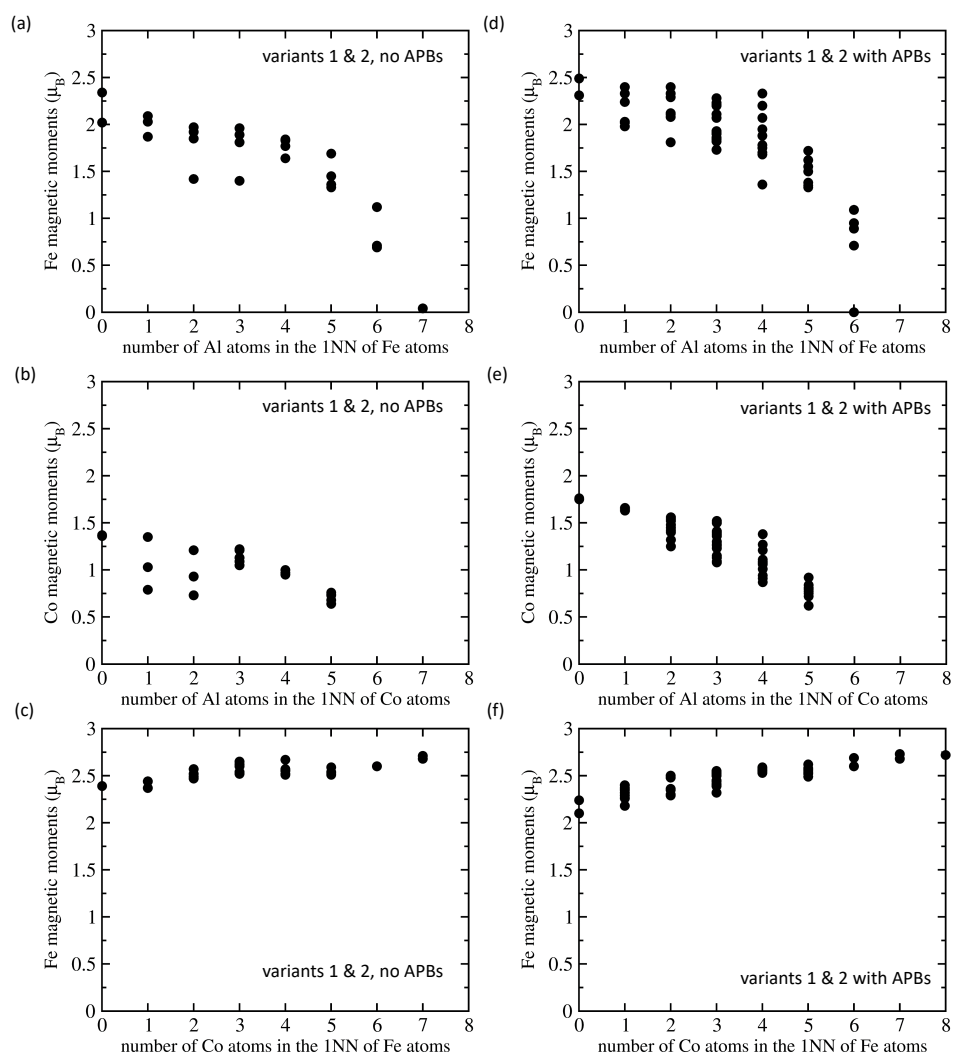


**Figure 4.** Calculated local magnetic moments of atoms (in Bohr magnetons,  $\mu_B$ ) as a function of the number of selected atoms in their first nearest neighbor shell (1NN) for supercells modeling  $\text{Fe}_2\text{CoAl}$  with and without APBs. In particular, for supercells without APBs, we show magnetic moment of Fe atoms from the (Fe,Co) sublattice as a function of the number of Al atoms in the 1NN of Fe atoms (a); magnetic moment of Co atoms from the (Fe,Co) sublattice as a function of the number of Al atoms in the 1NN of Co atoms (b); and magnetic moment of Fe atoms from the (Fe,Al) sublattice as a function of the number of Co atoms in the 1NN of Fe atoms (c). For supercells with APBs, we show magnetic moment of Fe atoms from the (Fe,Co) sublattice as a function of the number of Al atoms in the 1NN of Fe atoms (d); magnetic moment of Co atoms from the (Fe,Co) sublattice as a function of the number of Al atoms in the 1NN of Co atoms (e); and magnetic moment of Fe atoms from the (Fe,Al) sublattice as a function of the number of Co atoms in the 1NN of Fe atoms (f).

## 5. Conclusions

We performed a first-principles study on thermodynamic, structural, elastic, and magnetic properties of single-phase ferromagnetic Fe<sub>2</sub>CoAl with a chemically disordered B2-type lattice with and without antiphase boundaries (APBs). Following experimental work of Grover et al. [80], Fe<sub>2</sub>CoAl was modeled by two different 54-atom supercells with atoms on the two B2 sublattices distributed according to the special quasi-random structure (SQS) concept. Both models have very similar formation energies (−0.243 and −0.244 eV/atom), B2 structure lattice parameters (2.849 and 2.850 Å), magnetic moments (1.266 and 1.274 μ<sub>B</sub> per atom), practically identical elastic constants (C<sub>11</sub> = 245 GPa, C<sub>12</sub> = 141 GPa and C<sub>44</sub> = 132 GPa), and similar auxetic properties (the lowest Poisson ratio around −0.1). The APB interfaces have (001) crystallographic orientation and are characterized by a shift in the lattice along the ⟨111⟩ crystallographic direction. The averaged APB interface energies were found to be 199 and 310 mJ/m<sup>2</sup> for the two models, and the difference between the two values clearly illustrates the sensitivity of the APB interface energy to the local atomic configuration at the interface. The studied APBs increased the total magnetic moment by 6 and 8% when compared with their corresponding APB-free states. This increase can be partly explained by differences in the volume and partly by rather complex APB-related changes in the coordination of magnetic atoms in the studied disordered system. In particular, we noted that the magnetic moment of Fe atoms was reduced by an increasing number of Al first nearest neighbors but was increased by the presence of Co first nearest neighbors. The APBs also enhanced the single-crystal auxetic properties when the minimum Poisson ratio was more negative due to the presence of APBs (changed from −0.083 to −0.139 and from −0.075 to −0.125 for variants 1 and 2, respectively).

**Author Contributions:** Writing—original draft preparation and visualization: M.F.; conceptualization and methodology: J.G., J.P., M.F. and M.Š.; writing—review and editing: M.F., J.G., J.P. and M.Š.; resources, project administration, and funding acquisition: M.F.; supervision: M.Š. All authors have read and agreed to the published version of the manuscript.

**Funding:** The authors acknowledge the Czech Science Foundation for the financial support received under the Project No. 20-08130S (M.Š. and M.F.).

**Institutional Review Board Statement:** Not applicable.

**Informed Consent Statement:** Not applicable.

**Data Availability Statement:** The data presented in this study are available on request from the corresponding author.

**Acknowledgments:** Computational resources were provided by the Ministry of Education, Youth and Sports of the Czech Republic under the Projects e-INFRA CZ (ID:90140) at the IT4Innovations National Supercomputing Center and e-Infrastruktura CZ (e-INFRA LM2018140) at the MetaCentrum as well as the CERIT-Scientific Cloud (Project No. LM2015085), all granted within the program Projects of Large Research, Development and Innovations Infrastructures. M.F. and M.Š. acknowledge the support provided by the Czech Academy of Sciences (project No. UFM-A-RVO:68081723). Figures 1 and 3 were visualized using VESTA [118].

**Conflicts of Interest:** The authors declare no conflicts of interest.

## References

1. Heusler, F.; Starck, W.; Haupt, E. Über magnetische Manganlegierungen. *Verh. Dtsch. Phys. Ges.* **1903**, *5*, 219.
2. Webster, P. Heusler Alloys. *Contemp. Phys.* **1969**, *10*, 559–577. [[CrossRef](#)]
3. Graf, T.; Felser, C.; Parkin, S.S.P. Simple rules for the understanding of Heusler compounds. *Prog. Solid State Chem.* **2011**, *39*, 1–50. [[CrossRef](#)]
4. Picozzi, S.; Continenza, A.; Freeman, A. Co<sub>2</sub>MnX (X=Si, Ge, Sn) Heusler compounds: An ab initio study of their structural, electronic, and magnetic properties at zero and elevated pressure. *Phys. Rev. B* **2002**, *66*, 094421. [[CrossRef](#)]
5. Webster, P. Magnetic and chemical order in Heusler alloys containing cobalt and manganese. *J. Phys. Chem. Solids* **1971**, *32*, 1221. [[CrossRef](#)]

6. Kübler, J.; Williams, A.; Sommers, C. Formation and coupling of magnetic-moments in Heusler alloys. *Phys. Rev. B* **1983**, *28*, 1745–1755. [[CrossRef](#)]
7. Galanakis, I.; Dederichs, P.H.; Papanikolaou, N. Slater-Pauling behavior and origin of the half-metallicity of the full-Heusler alloys. *Phys. Rev. B* **2002**, *66*, 174429. [[CrossRef](#)]
8. Miura, Y.; Nagao, K.; Shirai, M. Atomic disorder effects on half-metallicity of the full-Heusler alloys  $\text{Co}_2(\text{Cr}_{1-x}\text{Fe}_x)\text{Al}$ : A first-principles study. *Phys. Rev. B* **2004**, *69*, 144413. [[CrossRef](#)]
9. Galanakis, I.; Dederichs, P.H.; Papanikolaou, N. Origin and properties of the gap in the half-ferromagnetic Heusler alloys. *Phys. Rev. B* **2002**, *66*, 134428. [[CrossRef](#)]
10. Kandpal, H.C.; Fecher, G.H.; Felser, C. Calculated electronic and magnetic properties of the half-metallic, transition metal based Heusler compounds. *J. Phys. D Appl. Phys.* **2007**, *40*, 1507–1523. [[CrossRef](#)]
11. Galanakis, I.; Mavropoulos, P.; Dederichs, P.H. Electronic structure and Slater-Pauling behaviour in half-metallic Heusler alloys calculated from first principles. *J. Phys. D Appl. Phys.* **2006**, *39*, 765–775. [[CrossRef](#)]
12. Buschow, K.; Van Engen, P. Magnetic and magneto-optical properties of Heusler alloys based on aluminum and gallium. *J. Magn. Magn. Mater.* **1981**, *25*, 90–96. [[CrossRef](#)]
13. Chadov, S.; Qi, X.; Kübler, J.; Fecher, G.H.; Felser, C.; Zhang, S.C. Tunable multifunctional topological insulators in ternary Heusler compounds. *Nat. Mater.* **2010**, *9*, 541–545. [[CrossRef](#)]
14. Lin, H.; Wray, L.A.; Xia, Y.; Xu, S.; Jia, S.; Cava, R.J.; Bansil, A.; Hasan, M.Z. Half-Heusler ternary compounds as new multifunctional experimental platforms for topological quantum phenomena. *Nat. Mater.* **2010**, *9*, 546–549. [[CrossRef](#)]
15. Planes, A.; Manosa, L.; Acet, M. Magnetocaloric effect and its relation to shape-memory properties in ferromagnetic Heusler alloys. *J. Phys. Condens. Matter* **2009**, *21*, 233201. [[CrossRef](#)]
16. Entel, P.; Buchelnikov, V.; Khovailo, V.; Zayak, A.; Adeagbo, W.; Gruner, M.; Herper, H.; Wassermann, E. Modelling the phase diagram of magnetic shape memory Heusler alloys. *J. Phys. D Appl. Phys.* **2006**, *39*, 865–889. [[CrossRef](#)]
17. Gilleßen, M.; Dronskowski, R. A combinatorial study of full Heusler alloys by first-principles computational methods. *J. Comput. Chem.* **2009**, *30*, 1290. [[CrossRef](#)]
18. Gilleßen, M.; Dronskowski, R. A combinatorial study of inverse Heusler alloys by first-principles computational methods. *J. Comput. Chem.* **2010**, *31*, 612. [[CrossRef](#)]
19. Sauthoff, G. *Intermetallics*; VCH Verlagsgesellschaft: Weinheim, Germany, 1995.
20. Liu, C.T.; Stringer, J.; Mundy, J.N.; Horton, L.L.; Angelini, P. Ordered intermetallic alloys: An assessment. *Intermetallics* **1997**, *5*, 579–596. [[CrossRef](#)]
21. Stoloff, N.S. Iron aluminides: Present status and future prospects. *Mater. Sci. Eng. A* **1998**, *258*, 1–14. [[CrossRef](#)]
22. Liu, C.T.; Lee, E.H.; McKamey, C.G. An environmental-effect as the major cause for room-temperature embrittlement in FeAl. *Scr. Metall. Mater.* **1989**, *23*, 875–880. [[CrossRef](#)]
23. Lynch, R.J.; Heldt, L.A.; Milligan, W.W. Effects of alloy composition on environmental embrittlement of B2 ordered iron aluminides. *Scr. Metall. Mater.* **1991**, *25*, 2147–2151. [[CrossRef](#)]
24. Liu, C.T.; McKamey, C.G.; Lee, E.H. Environmental-effects on room-temperature ductility and fracture in  $\text{Fe}_3\text{Al}$ . *Scr. Metall. Mater.* **1990**, *24*, 385–389. [[CrossRef](#)]
25. Lynch, R.J.; Gee, K.A.; Heldt, L.A. Environmental embrittlement of single-crystal and thermomechanically processed B2-ordered iron aluminides. *Scr. Metall. Mater.* **1994**, *30*, 945–950. [[CrossRef](#)]
26. Zamanzade, M.; Barnoush, A.; Motz, C. A review on the properties of iron aluminide intermetallics. *Crystals* **2016**, *6*, 10. [[CrossRef](#)]
27. Kattner, U.; Burton, B. Al-Fe (Aluminium-Iron). In *Phase Diagrams of Binary Iron Alloys*; Okamoto, H., Ed.; ASM International: Materials Park, OH, USA, 1993; pp. 12–28.
28. Palm, M.; Inden, G.; Thomas, N. The Fe-Al-Ti system. *J. Phase Equilibria* **1995**, *16*, 209–222. [[CrossRef](#)]
29. Vernieres, J.; Benelmekki, M.; Kim, J.H.; Grammatikopoulos, P.; Bobo, J.F.; Diaz, R.E.; Sowwan, M. Single-step gas phase synthesis of stable iron aluminide nanoparticles with soft magnetic properties. *APL Mater.* **2014**, *2*, 116105. [[CrossRef](#)]
30. Jirásková, Y.; Pizúrová, N.; Titov, A.; Janičkovič, D.; Friák, M. Phase separation in Fe-Ti-Al alloy—Structural, magnetic, and Mössbauer study. *J. Magn. Magn. Mater.* **2018**, *468*, 91–99. [[CrossRef](#)]
31. Palm, M.; Lacaze, J. Assessment of the Al-Fe-Ti system. *Intermetallics* **2006**, *14*, 1291–1303. [[CrossRef](#)]
32. Dobeš, F.; Dymáček, P.; Friák, M. Force-to-stress conversion methods in small punch testing exemplified by creep results of Fe-Al alloy with chromium and cerium additions. *IOP Conf. Ser. Mater. Sci. Eng.* **2018**, *461*, 012017. [[CrossRef](#)]
33. Dobeš, F.; Dymáček, P.; Friák, M. Small punch creep of Fe-Al-Cr alloy with Ce addition and its relation to uniaxial creep tests. *Met. Mater. Kovové Mater.* **2018**, *56*, 205. [[CrossRef](#)]
34. Palm, M.; Sauthoff, G. Deformation behaviour and oxidation resistance of single-phase and two-phase  $\text{L}_{21}$ -ordered Fe-Al-Ti alloys. *Intermetallics* **2004**, *12*, 1345–1359. [[CrossRef](#)]
35. Sundman, B.; Ohnuma, I.; Dupin, N.; Kattner, U.R.; Fries, S.G. An assessment of the entire Al-Fe system including  $\text{D}_{03}$  ordering. *Acta Mater.* **2009**, *57*, 2896–2908. [[CrossRef](#)]
36. Dymáček, P.; Dobeš, F.; Jirásková, Y.; Pizúrová, N.; Friák, M. Tensile, creep and fracture testing of prospective Fe-Al-based alloys using miniature specimens. *Theor. Appl. Fract. Mech.* **2019**, *99*, 18–26. [[CrossRef](#)]

37. Dobeš, F.; Dymáček, P.; Friák, M. The influence of niobium additions on creep resistance of Fe-27 at. % Al alloys. *Metals* **2019**, *9*, 739. [[CrossRef](#)]
38. Grigorichik, A.N.; Astrashab, V.E.; Kukareko, V.A.; Belotserkovsky, M.A.; Sosnovsky, V.A. High-temperature heat treatment of hypersonic metallization coatings from pseudoalloy “Fe-Al”. *Lett. Mater.* **2021**, *11*, 198–203. [[CrossRef](#)]
39. Deevi, S.C. Advanced intermetallic iron aluminide coatings for high temperature applications. *Prog. Mater. Sci.* **2021**, *118*, 100769. [[CrossRef](#)]
40. Tolochyn, O.I.; Baglyuk, G.A.; Tolochyna, O.V.; Evyeh, Y.I.; Podrezov, Y.M.; Molchanovska, H.M. Structure and physicochemical properties of the Fe<sub>3</sub>Al intermetallic compound obtained by impact hot compaction. *Mater. Sci.* **2021**, *56*, 499–508. [[CrossRef](#)]
41. Komarov, O.N.; Zhilin, S.G.; Predein, V.V.; Popov, A.V. Mechanisms for forming iron-containing intermetallics prepared by aluminothermy and the effect of special treatment methods on their properties. *Metallurgist* **2020**, *64*, 810–821. [[CrossRef](#)]
42. Vodičková, V.; Švec, M.; Hanus, P.; Novák, P.; Záděra, A.; Keller, V.; Prokopčáková, P.P. The effect of simultaneous Si and Ti/Mo alloying on high-temperature strength of Fe<sub>3</sub>Al-based iron aluminides. *Molecules* **2020**, *25*, 4268. [[CrossRef](#)]
43. Luo, X.; Cao, J.; Meng, G.; Chuan, Y.; Yao, Z.; Xie, H. Systematical investigation on the microstructures and tribological properties of Fe-Al laser cladding coatings. *Appl. Surf. Sci.* **2020**, *516*, 146121. [[CrossRef](#)]
44. Luo, X.; Cao, J.; Meng, G.; Yu, F.; Jiang, Q.; Zhang, P.; Xie, H. Double glow plasma surface metallurgy technology fabricated Fe-Al-Cr coatings with excellent corrosion resistance. *Coatings* **2020**, *10*, 575. [[CrossRef](#)]
45. Teker, T.; Yilmaz, S.O. Synthesis and structural characterization of Fe based Ti+Ni<sub>3</sub>Al+Al<sub>2</sub>O<sub>3</sub> reinforcement composite produced by mechanical alloying. *Rev. Metal.* **2020**, *56*, 4. [[CrossRef](#)]
46. Zhang, X.; Sun, Y.; Niu, M.; Shao, M.; Geng, X. Microstructure and mechanical behavior of in situ TiC reinforced Fe<sub>3</sub>Al (Fe-23Al-3Cr) matrix composites by mechanical alloying and vacuum hot-pressing sintering technology. *Vacuum* **2020**, *180*, 109544. [[CrossRef](#)]
47. Ghazanfari, H.; Blais, C.; Garipey, M.; Savoie, S.; Schulz, R.; Alamdari, H. Improving wear resistance of metal matrix composites using reinforcing particles in two length-scales: Fe<sub>3</sub>Al/TiC composites. *Surf. Coat. Technol.* **2020**, *386*, 125502. [[CrossRef](#)]
48. Khodaei, M. Characterization of Al<sub>2</sub>O<sub>3</sub> in Fe<sub>3</sub>Al-30 vol.% Al<sub>2</sub>O<sub>3</sub> nanocomposite powder synthesized by mechanochemical process. *J. Nanostruct.* **2020**, *10*, 456–462. [[CrossRef](#)]
49. Altunin, R.R.; Moiseenko, E.T.; Zharkov, S.M. Structural phase transformations during a solid-state reaction in a bilayer Al/Fe thin-film nanosystem. *Phys. Solid State* **2020**, *62*, 200–205. [[CrossRef](#)]
50. Tolochyn, O.I.; Tolochyna, O.V.; Baglyuk, H.A.; Yevych, Y.I.; Podrezov, Y.M.; Mamonova, A.A. Influence of sintering temperature on the structure and properties of powder iron aluminide Fe<sub>3</sub>Al. *Powder Metall. Met. Ceram.* **2020**, *59*, 150–159. [[CrossRef](#)]
51. Adler, L.; Fu, Z.; Koerner, C. Electron beam based additive manufacturing of Fe<sub>3</sub>Al based iron aluminides—Processing window, microstructure and properties. *Mater. Sci. Eng. A* **2020**, *785*, 139369. [[CrossRef](#)]
52. Michalcová, A.; Ozkan, M.; Mikula, P.; Marek, I.; Knaislová, A.; Kopeček, J.; Vojtěch, D. The influence of powder milling on properties of SPS compacted FeAl. *Molecules* **2020**, *25*, 2263. [[CrossRef](#)]
53. Peska, M.; Karczewski, K.; Rzeszutarska, M.; Polanski, M. Direct synthesis of Fe-Al alloys from elemental powders using laser engineered net shaping. *Materials* **2020**, *13*, 531. [[CrossRef](#)]
54. Luo, X.; Cao, J.; Meng, G.; Zhou, Y.; Xie, H. Long-range-ordered Fe<sub>3</sub>Al with excellent electromagnetic wave absorption. *J. Mater. Sci. Mater. Electron.* **2020**, *31*, 15608–15615. [[CrossRef](#)]
55. Ismail, A.; Bahanan, W.; Bin Hussain, P.; Saat, A.M.; Shaik, N.B. Diffusion bonding of Al-Fe enhanced by gallium. *Processes* **2020**, *8*, 824. [[CrossRef](#)]
56. Watson, R.E.; Weinert, M. Transition-metal aluminide formation: Ti, V, Fe, and Ni aluminides. *Phys. Rev. B* **1998**, *58*, 5981–5988. [[CrossRef](#)]
57. Gonzales-Ormeno, P.; Petrilli, H.; Schön, C. Ab-initio calculations of the formation energies of BCC-based superlattices in the Fe-Al system. *Calphad* **2002**, *26*, 573–582. [[CrossRef](#)]
58. Connetable, D.; Maugis, P. First principle calculations of the kappa-Fe<sub>3</sub>AlC perovskite and iron-aluminium intermetallics. *Intermetallics* **2008**, *16*, 345–352. [[CrossRef](#)]
59. Kellou, A.; Grosdidier, T.; Raulot, J.M.; Aourag, H. Atomistic study of magnetism effect on structural stability in Fe<sub>3</sub>Al and Fe<sub>3</sub>AlX (X = H, B, C, N, O) alloys. *Phys. Status Solidi B Basic Solid State Phys.* **2008**, *245*, 750–755. [[CrossRef](#)]
60. Šesták, P.; Friák, M.; Holec, D.; Všíanská, M.; Šob, M. Strength and brittleness of interfaces in Fe-Al superalloy nanocomposites under multiaxial loading: An ab initio and atomistic study. *Nanomaterials* **2018**, *8*, 873. [[CrossRef](#)]
61. Lechermann, F.; Fähnle, M.; Meyer, B.; Elsässer, C. Electronic correlations, magnetism, and structure of Fe-Al subsystems: An LDA + U study. *Phys. Rev. B* **2004**, *69*, 165116. [[CrossRef](#)]
62. Airiskallio, E.; Nurmi, E.; Heinonen, M.H.; Vayrynen, I.J.; Kokko, K.; Ropo, M.; Punkkinen, M.P.J.; Pitkanen, H.; Alatalo, M.; Kollar, J.; et al. High temperature oxidation of Fe-Al and Fe-Cr-Al alloys: The role of Cr as a chemically active element. *Corros. Sci.* **2010**, *52*, 3394–3404. [[CrossRef](#)]
63. Lechermann, F.; Welsch, F.; Elsässer, C.; Ederer, C.; Fähnle, M.; Sanchez, J.; Meyer, B. Density-functional study of Fe<sub>3</sub>Al: LSDA versus GGA. *Phys. Rev. B* **2002**, *65*, 132104. [[CrossRef](#)]
64. Friák, M.; Slávik, A.; Miháliková, I.; Holec, D.; Všíanská, M.; Šob, M.; Palm, M.; Neugebauer, J. Origin of the low magnetic moment in Fe<sub>2</sub>AlTi: An Ab initio study. *Materials* **2018**, *11*, 1732. [[CrossRef](#)]

65. Ju, J.; Kang, M.; Zhou, Y.; Yang, C.; Wang, K.; Li, J.; Wang, R.; Fu, H.; Wang, J. First-principles investigations of the stability, electronic structures, mechanical properties and thermodynamic properties of  $\text{Fe}_x\text{Al}_y\text{C}_z$  compounds in Fe-Cr-B-Al-C alloy. *J. Phys. Chem. Solids* **2020**, *143*, 109366. [[CrossRef](#)]
66. Miháliková, I.; Friák, M.; Jirásková, Y.; Holec, D.; Koutná, N.; Šob, M. Impact of nano-scale distribution of atoms on electronic and magnetic properties of phases in Fe-Al nanocomposites: An ab initio study. *Nanomaterials* **2018**, *8*, 1059. [[CrossRef](#)] [[PubMed](#)]
67. Friák, M.; Holec, D.; Šob, M. Quantum-mechanical study of nanocomposites with low and ultra-low interface energies. *Nanomaterials* **2018**, *8*, 1057. [[CrossRef](#)] [[PubMed](#)]
68. Kulikov, N.I.; Postnikov, A.V.; Borstel, G.; Braun, J. Onset of magnetism in B2 transition-metal aluminides. *Phys. Rev. B* **1999**, *59*, 6824–6833. [[CrossRef](#)]
69. Friák, M.; Neugebauer, J. Ab initio study of the anomalous volume-composition dependence in Fe-Al alloys. *Intermetallics* **2010**, *18*, 1316–1321. [[CrossRef](#)]
70. Ipsier, H.; Semenova, O.; Krachler, R. Intermetallic phases with  $\text{D}_{03}$ -structure: A statistical-thermodynamic model. *J. Alloy. Compd.* **2002**, *338*, 20–25. [[CrossRef](#)]
71. Fähnle, M.; Drautz, R.; Lechermann, F.; Singer, R.; Diaz-Ortiz, A.; Dosch, H. Thermodynamic properties from ab-initio calculations: New theoretical developments, and applications to various materials systems. *Phys. Status Solidi B Basic Solid State Phys.* **2005**, *242*, 1159–1173. [[CrossRef](#)]
72. Kirklin, S.; Saal, J.E.; Hegde, V.I.; Wolverton, C. High-throughput computational search for strengthening precipitates in alloys. *Acta Mater.* **2016**, *102*, 125–135. [[CrossRef](#)]
73. Liu, S.; Duan, S.; Ma, B. First-principles calculation of vibrational entropy for Fe-Al compounds. *Phys. Rev. B* **1998**, *58*, 9705–9709.
74. Čížek, J.; Lukáč, F.; Procházka, I.; Kužel, R.; Jirásková, Y.; Janičkovič, D.; Anwand, W.; Brauer, G. Characterization of quenched-in vacancies in Fe-Al alloys. *Physica B* **2012**, *407*, 2659–2664. [[CrossRef](#)]
75. Miháliková, I.; Friák, M.; Koutná, N.; Holec, D.; Šob, M. An ab initio study of vacancies in disordered magnetic systems: A case study of Fe-rich Fe-Al phases. *Materials* **2019**, *12*, 1430. [[CrossRef](#)]
76. Amara, H.; Fu, C.C.; Soisson, F.; Maugis, P. Aluminum and vacancies in  $\alpha$ -iron: Dissolution, diffusion, and clustering. *Phys. Rev. B* **2010**, *81*, 174101. [[CrossRef](#)]
77. Friák, M.; Černý, M.; Všianská, M.; Šob, M. Impact of antiphase boundaries on structural, magnetic and vibrational properties of  $\text{Fe}_3\text{Al}$ . *Materials* **2020**, *13*, 4884. [[CrossRef](#)]
78. Li, Y.; Liu, Y.; Yang, J. First principle calculations and mechanical properties of the intermetallic compounds in a laser welded steel/aluminum joint. *Opt. Laser Technol.* **2020**, *122*, 105875. [[CrossRef](#)]
79. Friák, M.; Černý, M.; Šob, M. The effect of hydrogen on the stress-strain response in  $\text{Fe}_3\text{Al}$ : An ab initio molecular-dynamics study. *Materials* **2021**, *14*, 4155. [[CrossRef](#)]
80. Grover, A.K.; Pillay, R.G.; Nagarajan, V.; Tandon, P.N. Site preference and local environment effects in ferromagnetic ternary alloys. *J. Magn. Magn. Mater.* **1980**, *15*, 699–700. [[CrossRef](#)]
81. Marcinkowski, M.; Brown, N. Theory and direct observation of dislocations in the  $\text{Fe}_3\text{Al}$  superlattices. *Acta Metall.* **1961**, *9*, 764–786. [[CrossRef](#)]
82. Marcinkowski, M.J.; Brown, N. Direct observation of antiphase boundaries in the  $\text{Fe}_3\text{Al}$  superlattice. *J. Appl. Phys.* **1962**, *33*, 537–552. [[CrossRef](#)]
83. Wang, K.; Wang, Y. The partitioning behavior of dual solutes at the antiphase domain boundary in the B2 intermetallic: A microscopic phase-field study. *J. Alloy. Compd.* **2020**, *824*, 153923. [[CrossRef](#)]
84. Koizumi, Y.; Allen, S.M.; Ouchi, M.; Minamino, Y. Effects of solute and vacancy segregation on antiphase boundary migration in stoichiometric and Al-rich  $\text{Fe}_3\text{Al}$ : A phase-field simulation study. *Intermetallics* **2010**, *18*, 1297–1302. [[CrossRef](#)]
85. Koizumi, Y.; Allen, S.M.; Minamino, Y. Effects of solute and vacancy segregation on migration of  $a/4\langle 111 \rangle$  and  $a/2\langle 100 \rangle$  antiphase boundaries in  $\text{Fe}_3\text{Al}$ . *Acta Mater.* **2009**, *57*, 3039–3051. [[CrossRef](#)]
86. Koizumi, Y.; Allen, S.M.; Ouchi, M.; Minamino, Y.; Chiba, A. Phase-field simulation of  $\text{D}_{03}$ -type antiphase boundary migration in  $\text{Fe}_3\text{Al}$  with vacancy and solute segregation. *Solid State Phenom.* **2011**, *172*, 1313–1319. [[CrossRef](#)]
87. Allen, S.; Cahn, J. Microscopic theory for antiphase boundary motion and its application to antiphase domain coarsening. *Acta Metall.* **1979**, *27*, 1085–1095. [[CrossRef](#)]
88. Wang, K.; Wang, Y.; Cheng, Y. The formation and dynamic evolution of antiphase domain boundary in FeAl alloy: Computational simulation in atomic scale. *Mater. Res. Ibero-Am. J. Mater.* **2018**, *21*, e20171048. [[CrossRef](#)]
89. Balagurov, A.M.; Bobrikov, I.A.; Sumnikov, V.S.; Golovin, I.S. Antiphase domains or dispersed clusters? Neutron diffraction study of coherent atomic ordering in  $\text{Fe}_3\text{Al}$ -type alloys. *Acta Mater.* **2018**, *153*, 45–52. [[CrossRef](#)]
90. Murakami, Y.; Niitsu, K.; Tanigaki, T.; Kainuma, R.; Park, H.S.; Shindo, D. Magnetization amplified by structural disorder within nanometre-scale interface region. *Nat. Commun.* **2014**, *5*, 4133. [[CrossRef](#)] [[PubMed](#)]
91. Oguma, R.; Matsumura, S.; Eguchi, T. Kinetics of B2- and  $\text{D}_{03}$  type ordering and formation of domain structures in Fe-Al alloys. *J. Phys. Condens. Matter* **2008**, *20*, 275225. [[CrossRef](#)] [[PubMed](#)]
92. Friák, M.; Všianská, M.; Šob, M. A quantum-mechanical study of clean and Cr-segregated antiphase boundaries in  $\text{Fe}_3\text{Al}$ . *Materials* **2019**, *12*, 3954. [[CrossRef](#)]
93. Friák, M.; Buršíková, V.; Pizúrová, N.; Pavlů, J.; Jirásková, Y.; Homola, V.; Miháliková, I.; Slávik, A.; Holec, D.; Všianská, M.; et al. Elasticity of phases in Fe-Al-Ti superalloys: Impact of atomic order and anti-phase boundaries. *Crystals* **2019**, *9*, 299. [[CrossRef](#)]

94. Friák, M.; Golian, M.; Holec, D.; Koutná, N.; Šob, M. An ab initio study of magnetism in disordered Fe-Al alloys with thermal antiphase boundaries. *Nanomaterials* **2020**, *10*, 44. [[CrossRef](#)]
95. Friák, M.; Černý, M.; Šob, M. The impact of vibrational entropy on the segregation of Cu to antiphase boundaries in Fe<sub>3</sub>Al. *Magnetochemistry* **2021**, *7*, 108. [[CrossRef](#)]
96. Zunger, A.; Wei, S.; Ferreira, L.; Bernard, J. Special quasirandom structures. *Phys. Rev. Lett.* **1990**, *65*, 353–356. [[CrossRef](#)] [[PubMed](#)]
97. Oganov, A.R.; Glass, C.W. Crystal structure prediction using ab initio evolutionary techniques: Principles and applications. *J. Chem. Phys.* **2006**, *124*, 244704. [[CrossRef](#)] [[PubMed](#)]
98. Lyakhov, A.O.; Oganov, A.R.; Stokes, H.T.; Zhu, Q. New developments in evolutionary structure prediction algorithm USPEX. *Comput. Phys. Commun.* **2013**, *184*, 1172–1182. [[CrossRef](#)]
99. Oganov, A.R.; Lyakhov, A.O.; Valle, M. How evolutionary crystal structure prediction works—and why. *Accounts Chem. Res.* **2011**, *44*, 227–237. [[CrossRef](#)]
100. Kresse, G.; Hafner, J. Ab initio molecular dynamics for liquid metals. *Phys. Rev. B* **1993**, *47*, 558–561. [[CrossRef](#)] [[PubMed](#)]
101. Kresse, G.; Furthmüller, J. Efficient iterative schemes for ab initio total-energy calculations using a plane-wave basis set. *Phys. Rev. B* **1996**, *54*, 11169–11186. [[CrossRef](#)]
102. Hohenberg, P.; Kohn, W. Inhomogeneous electron gas. *Phys. Rev. B* **1964**, *136*, B864–B871. [[CrossRef](#)]
103. Kohn, W.; Sham, L.J. Self-consistent equations including exchange and correlation effects. *Phys. Rev. A* **1965**, *140*, A1133–A1138. [[CrossRef](#)]
104. Blöchl, P.E. Projector augmented-wave method. *Phys. Rev. B* **1994**, *50*, 17953–17979. [[CrossRef](#)] [[PubMed](#)]
105. Kresse, G.; Joubert, D. From ultrasoft pseudopotentials to the projector augmented-wave method. *Phys. Rev. B* **1999**, *59*, 1758–1775. [[CrossRef](#)]
106. Perdew, J.P.; Wang, Y. Accurate and simple analytic representation of the electron-gas correlation energy. *Phys. Rev. B* **1992**, *45*, 13244–13249. [[CrossRef](#)] [[PubMed](#)]
107. Vosko, S.H.; Wilk, L.; Nusair, M. Accurate spin-dependent electron liquid correlation energies for local spin density calculations: A critical analysis. *Can. J. Phys.* **1980**, *58*, 1200. [[CrossRef](#)]
108. Všíanská, M.; Friák, M.; Šob, M. An ab initio study of Fe<sub>3</sub>Al: A critical review of generalized gradient approximation. *Comp. Phys. Comm.* **2022**, to be published.
109. Friák, M.; Oweisová, S.; Pavlů, Jana Holec, D.; Šob, M. An ab initio study of thermodynamic and mechanical stability of Heusler-based Fe<sub>2</sub>AlCo polymorphs. *Materials* **2018**, *11*, 1543. [[CrossRef](#)]
110. Gracias, J. Ab Initio Modelling of Properties of Al<sub>3</sub>Fe<sub>13</sub> and Al<sub>4</sub>Co<sub>4</sub>Fe<sub>8</sub> Phase. Bachelor's Thesis, Masaryk University in Brno, Brno, Czech Republic, 2020. (In Czech)
111. von Pezold, J.; Dick, A.; Friak, M.; Neugebauer, J. Generation and performance of special quasirandom structures for studying the elastic properties of random alloys: Application to Al-Ti. *Phys. Rev. B* **2010**, *81*, 094203. [[CrossRef](#)]
112. Jain, V.; Nehra, J.; Sudheesh, V.D.; Nambakkat, L.; Venugopalan, K. Comparative study of the structural and magnetic properties of bulk and nano-sized Fe<sub>2</sub>CoAl. *AIP Conf. Proc.* **2013**, *1536*, 935. [[CrossRef](#)]
113. Moakher, M.; Norris, A.N. The closest elastic tensor of arbitrary symmetry to an elasticity tensor of lower symmetry. *J. Elast.* **2006**, *85*, 215–263. [[CrossRef](#)]
114. Gaillac, R.; Pullumbi, P.; Coudert, F.X. ELATE: An open-source online application for analysis and visualization of elastic tensors. *J. Phys. Condens. Matter* **2016**, *28*, 275201. [[CrossRef](#)] [[PubMed](#)]
115. Voigt, W. *Lehrbuch der Kristallphysik*; Teubner: Stuttgart, Germany, 1928.
116. Reuss, A. Account of the liquid limit of mixed crystals on the basis of the plasticity condition for single crystal. *Z. Angew. Math. Mech.* **1929**, *9*, 49–58. [[CrossRef](#)]
117. Hill, R. The elastic behaviour of a Ccystalline aggregate. *Proc. Phys. Soc. Sect. A* **1952**, *65*, 349–354. [[CrossRef](#)]
118. Momma, K.; Izumi, F. VESTA 3 for three-dimensional visualization of crystal, volumetric and morphology data. *J. Appl. Crystallogr.* **2011**, *44*, 1272–1276. [[CrossRef](#)]